

## Article

# Inter-Annual Climate Variability Impact on Oil Palm Mapping

Fernando Troya <sup>1,\*</sup>, Paulo N. Bernardino <sup>1</sup> and Ben Somers <sup>1,2</sup> 

<sup>1</sup> Division Forest, Nature and Landscape, KU Leuven, Celestijnenlaan 200E, 3001 Heverlee, Belgium; negribernardino.paulo@kuleuven.be (P.N.B.); ben.somers@kuleuven.be (B.S.)

<sup>2</sup> KU Leuven Plant Institute (LPI), Kasteelpark Arenberg 31, 3001 Heverlee, Belgium

\* Correspondence: fernando.troyaandrade@kuleuven.be

**Abstract:** The contribution of oil palm plantations to the economic growth of tropical developing countries makes it essential to monitor their expansion into the tropical forest; consequently, most studies focus on improving mapping accuracy while using satellite imagery. However, accuracy can be hampered by atmospheric phenomena that can drastically change climatic conditions in tropical regions, affecting the spectral properties of the vegetation. In this sense, we studied the accuracy of palm plantation mapping by using features from different regions of the electromagnetic spectrum and a data fusion approach, and then compared the changes in accuracy over the years 2016, 2017, and 2018 (two of them with reported climatic anomalies). Optical-based maps obtained higher accuracy than thermal- and microwave-based maps, but they were the most affected by inter-annual climate variability (error margin between 5 and 10%), while thermal-based maps were the least affected (error margin between 8 and 9%). Data fusion combinations improved accuracy and reduced dissimilarities between years (e.g., phenology-based map accuracy changed by up to 20.8%, while phenology fused with microwave features changed by up to 6.8%). We conclude that inter-annual climate variability on land-cover mapping should be considered, especially if the outputs will be used as input in future studies.

**Keywords:** mapping accuracy; oil palm; inter-annual climate variability; remote sensing; tropical forest; spectral region; data fusion; ENSO



**Citation:** Troya, F.; Bernardino, P.N.; Somers, B. Inter-Annual Climate Variability Impact on Oil Palm Mapping. *Remote Sens.* **2022**, *14*, 3104. <https://doi.org/10.3390/rs14133104>

Academic Editor:  
Arturo Sanchez-Azofeifa

Received: 21 April 2022

Accepted: 24 June 2022

Published: 28 June 2022

**Publisher's Note:** MDPI stays neutral with regard to jurisdictional claims in published maps and institutional affiliations.



**Copyright:** © 2022 by the authors. Licensee MDPI, Basel, Switzerland. This article is an open access article distributed under the terms and conditions of the Creative Commons Attribution (CC BY) license (<https://creativecommons.org/licenses/by/4.0/>).

## 1. Introduction

One of the most important and studied crops in tropical territories, mostly present on the industrial scale, is oil palm, especially due to its high impact in the economic development of tropical countries, but at the same time, also due to its relevant role in the degradation of natural ecosystems [1–3]. Oil palm plantation is a growing business around the world, driven by an increasing demand for palm oil over the last decades, mainly due to its versatility, e.g., used as raw material in the food and cosmetic industries and in the production of biodiesel [4,5]. Thus, palm oil represents one of the biggest pillars of economic growth in tropical developing countries. However, since it shares the same environmental and climatic requirements as lowland tropical rainforest [1], palm plantation is one of the main drivers of deforestation in the tropics, leading to biodiversity loss and the reduction of carbon storage, even inside the limits of protected forest areas [6].

Frequent mapping of palm plantation area is critical for the monitoring of the expansion of its frontier and for a correct management of forest resources. However, up-to-date information on land-cover changes is not common in these remote areas. Because field monitoring is complex and expensive, it does not allow for frequent updates across large regions. Conversely, satellite images can cover remote and extensive areas (at regional or national scale), offering a great advantage in comparison to field monitoring for assessing the impact of palm area expansion [6].

Remotely sensed optical spectra have proven to be useful for mapping land cover, through specific spectral signatures or spectral indices, both created with reflectance

data [7–10]. Thermal imagery has also shown to provide useful information to differentiate between forest and non-forest areas [11,12]. In tropical regions, however, the use of optical and thermal imagery is often complicated by excessive cloud coverage, hampering a continuous monitoring over large areas [13,14]. To address this limitation, SAR (Synthetic Aperture Radar) imagery [5,15–17] can be used to measure the surface backscatter in the microwave spectrum, as it is less affected by clouds.

Moreover, the fusion of spectral features from different spectral regions (i.e., optical, thermal, and microwave) has been reported to improve the accuracy and the spatial resolution of classification efforts [18–21]. Different data fusion techniques (e.g., pixel-based, object-based, or decision-level fusion [22,23]) and different classification algorithms (e.g., Random Forest, Support Vector Machine, and K-Nearest Neighbor [10,16,24]) have been tested to map palm plantations.

Nevertheless, previous studies tested their mapping approach in a single year, but as such, they failed to test the robustness of the methods to inter-annual climate variability. Such a test is important especially in the tropics, where atmospheric phenomena (e.g., the El Niño Southern Oscillation (ENSO) and the Pacific Decadal Oscillation) can drastically change climatic conditions [25].

In such situations, one can expect drastic changes in the rainfall and temperature regimes from one year to another [26], affecting the vegetation condition and, in turn, impacting the spectral properties (i.e., reflectance, emittance, and even backscattering) of the land surface components and, consequently, the mapping accuracy [11,17,27].

Therefore, to fill this gap, our study aims, first of all, to improve our understanding of satellite-based mapping of palm plantations by using features derived from distinct spectral regions (i.e., optical, thermal, and microwave) and a data-fusion approach. We analyzed how variations in climatic conditions might affect palm plantation mapping by evaluating the robustness of our mapping approach with respect to inter-annual climate variability observed across three different years. In this sense, we first focused on comparing the Overall Accuracy obtained by the annual classification maps created from these different features. Then, following the same methodology, we created three annual maps, corresponding to the three years analyzed, to study the changes in the output maps and their accuracies. Observed differences here are assumed to be mainly due to the effect of changing climate conditions.

## 2. Materials and Methods

### 2.1. Area of Study and Period

Ecuador is one of the major oil palm producers in Latin America [28], and its largest plantation area is located in the province of Esmeraldas, in the north of the coastal region (1°26'N–0°2'S and 78°22'W–80°10'W; Figure 1). Esmeraldas was once known as the Green Province due to the vast extension of its tropical forest, the Chocó forest, one of the world's biodiversity hotspots [29]. For this reason, the Ecuadorian government has created nine protected areas in its territory [30]. Nevertheless, it has suffered deforestation and a latter growing establishment of palm plantations in the last three decades [31,32]. Currently, it also has a high production of cocoa and banana, and large areas for livestock pasture [33]. Its topography is mostly flat, with elevation not surpassing 800 m above sea level in most of the territory [34], besides the southeast limit, which has borders with the Andes Mountains.

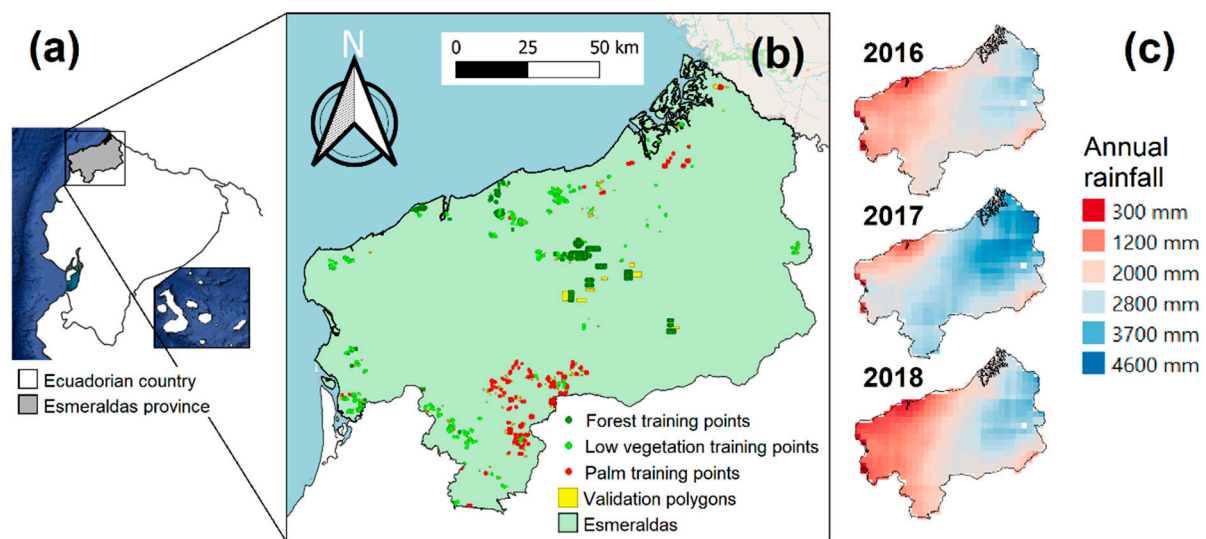


**Figure 1.** Delimitation of the area of study, comprising the Esmeraldas province (b), which is situated in the north of the coastal region of the Ecuadorian Republic (a). The central image shows the distribution of the sample points from which the spectral information is extracted to use it in the classifier. (c) Annual rainfall of the area of study during the years 2016, 2017, and 2018. Fluctuations among years are observed. Rainfall data retrieved from the Climate Hazards Group InfraRed Precipitation with Station (CHIRPS) dataset [35].

Esmeraldas presents three different types of climate: tropical sub-humid, humid, and very humid, with an average temperature around 23 °C [36]. However, the entire Ecuadorian coastal region is affected by several atmospheric phenomena, such as the ENSO and the Pacific Decadal Oscillation, that result in changes in precipitation, cloud cover, and air temperature [25].

In the present study, we used a three-year period (2016, 2017, and 2018) to assess the impact of distinct inter-annual precipitation regimes on our classification approach. The year of 2016 presented a drought, due to the occurrence of an ENSO event [37], with an average over the area of study of 2200 mm of annual rainfall, ranging from 540 to 3440 mm. In turn, 2017 was a regular year, with average rainfall levels over the area of study: mean annual rainfall of 2975 mm, ranging from 800 mm to more than 4600 mm. In 2018, an ENSO event affected the region again [38], reducing the mean annual rainfall to 2100 mm, which ranged from 340 to 3840 mm over the area of study (Figure 1c).

## 2.2. Satellite Imagery

We used imagery from the Moderate Resolution Imaging Spectroradiometer (MODIS) sensor (Table 1), a multispectral sensor that acquires images from 36 spectral bands, ranging from the optical to the thermal spectral region. The images have a coarse spatial resolution (250 m, 500 m, and 1 km pixel size) but high temporal resolution, with a revisit time of 1 to 2 days [39]. MODIS is onboard two different satellites, both producing images with the same characteristics: the Terra satellite, which passes the equator at 10:00 a.m.; and the Aqua satellite, which passes the equator at 1:30 p.m. [39,40].

In the present study, we followed a multi-temporal approach by using the MODIS database; in other words, we used all available images over a one-year period, i.e., 23 images in the case of the Vegetation Index product, and 46 in the case of Land Surface Reflectance and Land Surface Temperature and Emissivity products (Table 1). The multi-temporal approach has been reported to increase mapping accuracy in comparison with a single-date approach [21].

**Table 1.** List of the satellite imagery and products used in this study.

Sensor	Product	EM Region	Image Characteristics	Spatial and Temporal Resolution	# Scenes per Year	Acquisition Time (Julian Days)
MODIS Terra	MOD13Q1	Optical	Vegetation Index (VI)	250 m—16 days	23	001,017,033,049,065,081,097, 113,129,145,161,177,193,209, 225,241,257,273,289,305,321, 337,353
	MOD09A1	Optical	Land Surface Reflectance (LSR)	500 m—8 days	46	001,009,017,025,033,041,049, 057,065,073,081,089,097,105, 113,121,129,137,145,153,161, 169,177,185,193,201,209,217, 225,233,241,249,257,265,273, 281,289,297,305,313,321,329, 337,345,353,361
	MOD11A2	Thermal	Land Surface Temperature and Emissivity (LST)	1 km—8 days	46	001,009,017,025,033,041,049, 057,065,073,081,089,097,105, 113,121,129,137,145,153,161, 169,177,185,193,201,209,217, 225,233,241,249,257,265,273, 281,289,297,305,313,321,329, 337,345,353,361
MODIS Aqua	MYD13Q1	Optical	VI	250 m—16 days	23	009,025,041,057,073,089,105, 121,137,153,169,185,201,217, 233,249,265,281,297,313,329, 345,361
	MYD09A1	Optical	LSR	500 m—8 days	46	001,009,017,025,033,041,049, 057,065,073,081,089,097,105, 113,121,129,137,145,153,161, 169,177,185,193,201,209,217, 225,233,241,249,257,265,273, 281,289,297,305,313,321,329, 337,345,353,361
	MYD11A2	Thermal	LST	1 km—8 days	46	001,009,017,025,033,041,049, 057,065,073,081,089,097,105, 113,121,129,137,145,153,161, 169,177,185,193,201,209,217, 225,233,241,249,257,265,273, 281,289,297,305,313,321,329, 337,345,353,361
PALSAR 2	FNF	Microwave	Dual polarization (HH and HV)	25 m—1 per year	1	Ranging from 180 to 295

However, to deal with cloud contamination, we created composite images and combined features coming from both satellites (Terra and Aqua). Finally, we smoothed the data by using the Savitzky–Golay (S–G) filter, adjusting its parameters (e.g., window size and number of envelop iterations) to remove outliers but preserving the main characteristics of the data (e.g., relative minimum and maximum), as better explained in the following paragraphs. The S–G filter was applied by using the TIMESAT software [41,42].

We also used the microwave images from the Phased Array type L-band Synthetic Aperture Radar 2 (PALSAR 2), which provides fine-beam dual-polarization images. The specific band (L-band) and polarizations (HH and HV) of PALSAR 2 allows it to penetrate the canopy and differentiate between forest and other land-cover types [43]. However, PALSAR 2 is a sensor with commercial purposes, meaning that the images are not free. To deal with this limitation, we used the features provided with the Forest/Non-Forest (FNF) annual map product [44], which is a classification map of forest and non-forest land cover of 25 m spatial resolution; this product includes a global mosaic of SAR features, which are freely available to download at the JAXA website ([https://www.eorc.jaxa.jp/ALOS/en/palsar\\_fnf/data/index.htm](https://www.eorc.jaxa.jp/ALOS/en/palsar_fnf/data/index.htm), accessed on 4 January 2021). This also implies that the map created with SAR data, contrary to MODIS data, follows a single-date approach.

### 2.3. Preprocessing

In total, we tested eleven approaches, six of them using features from a single spectral region and five using a data-fusion approach that combines features from different spectral regions. Three of the evaluated approaches used optical features: (i) a vegetation-index approach (VI), (ii) a phenology-metrics approach (PHENO), and (iii) a spectral-reflectance approach (SRB).

VI uses mathematical equations created to summarize the information contained in different spectral bands to facilitate the analysis of intra-annual changes in

vegetation [9,45]. We followed a multi-index method [8] that incorporates different information from the land cover provided by different Vegetation Indices. We combined the widely used NDVI (Normalized Difference Vegetation Index) with EVI (Enhanced Vegetation Index), both related to photosynthetic activity, and both retrieved directly from MOD13Q1 and MYD13Q1 products, calculated according to the following formulas:

$$\text{NDVI} = (\text{NIR} - \text{red}) / (\text{NIR} + \text{red}) \quad (1)$$

$$\text{EVI} = 2.5 \times (\text{NIR} - \text{red}) / (\text{NIR} + \text{C1} \times \text{red} - \text{C2} \times \text{blue} + \text{L}) \quad (2)$$

Both NDVI and EVI consist in the ratio of the red band (wavelength: 620 to 670  $\mu\text{m}$ ), which is related to photosynthetic activity, and NIR band (wavelength: 841 to 876  $\mu\text{m}$ ), which is related to leaf/canopy structure. In the case of EVI, adjustment factors are included ( $\text{L} = 1$ ,  $\text{C1} = 6$ , and  $\text{C2} = 7.5$ ) to make EVI less prone to saturation in densely vegetated areas, as is the case with NDVI; however, EVI is more sensitive to variations in viewing geometry [46].

We also include the NDII (Normalized Difference Infrared Index), which was computed with the following equation:

$$\text{NDII} = (\text{NIR} - \text{SWIR7}) / (\text{NIR} + \text{SWIR7}) \quad (3)$$

The NDII index used the SWIR7 band (wavelength: 2105 to 2155  $\mu\text{m}$ ), which is sensitive to the water content in vegetation [47]. Knowing that cloud presence results in sudden drops in Vegetation Index values [48], after combining the images from both satellites (i.e., a total of 46 images per year), we applied the S–G filter, setting the window size to 10 and the number of envelope iterations to 3 in order to filter out extremely low values and keep the high ones.

PHENO uses the time series of the three Vegetation Indices used in the VI approach to extract phenology metrics [42]. We extracted these metrics from the fitted time series by using the S–G filter and 20% of the seasonal amplitude to establish the start of the season. We fed the classification algorithm with the thirteen metrics that TIMESAT allowed us to extract: time and value of the start and end of the season; base value, length, and amplitude of the season; large and small growing season integrals; value and time of the peak of the season; and left and right derivatives.

SRB uses the reflectance values from all available optical spectral bands. This approach is most common when using the Landsat dataset [2,7,10], and it consists of using raw spectral information from all the bands to differentiate among land-cover types through their multispectral signatures. We used two different MODIS products (Table 1), totaling seven optical spectral bands (i.e., blue, green, red, NIR, SWIR5, SWIR6, and SWIR7). Contrary to the case of Vegetation Indices, cloud contamination produces higher reflectance values than expected from vegetation in all spectral bands [49]. Therefore, during the preprocessing of the spectral bands coming from the Vegetation Index product (i.e., blue, red, NIR, and SWIR7), we combined the images from both satellites and created a composite, keeping pixels with the lowest values, (corresponding to the highest absorption), resulting in 23 images per band and per year. Then all images were smoothed with the S–G filter, adjusting the window size to 4 and the number of envelope iterations to 1, this time to filter out extremely high values and keep the low ones. In the case of the bands from the Land Surface Reflectance product (i.e., green, SWIR5, and SWIR6), we combined the images from the Terra and the Aqua satellites and then created composites, keeping the pixels with the lowest values, resulting again in 23 images per band and per year. Finally, we smoothed the data with the S–G filter, adjusting the parameters in the same way as with the Vegetation Index product.

The fourth and fifth approaches evaluated used the thermal spectral bands from the MODIS instrument. More specifically, we used (iv) the Daytime Surface Temperature (DST) and (v) the Nighttime Surface Temperature (NST) features. The thermal bands are also highly affected by cloud contamination, which impacts the retrieval of surface emittance



data by the MODIS sensors, preventing the derivation of the Land Surface Temperature and Emissivity (LST) product (Table 1) in contaminated pixels [39]. To address the lack of data, we combined both sources (Terra and Aqua satellites) to create composite images (i.e., 46 images per year), keeping pixels with the highest values, although we expected to find small differences in the temperature due to the different acquisition times. MODIS LST products have a pixel size of 1 km. Thus, to combine this product with features from different spectral regions (described before), we resampled the images to 250 m, using the bilinear method [4]. Finally, we applied the S–G filter—in this case, to preserve original values and, at the same time, fill in missing values in the time series through interpolation. We set the window size to 2 and the number of envelope iterations to 1.

The sixth approach assessed was (vi) the microwave feature approach (hereafter, SAR map); in order to create the SAR map, we masked low-quality pixels (with shadows or lay-over issues) and generated two new features: the ratio (HH/HV) and the difference (HH – HV) between both polarization images [16]. Then we removed the speckle effect by applying the Refined Lee speckle filter [50] on the Sentinel Application Platform (SNAP) [51]. Next, we resampled the features to a 250 m resolution, using the bilinear method, since it has been reported that an increased accuracy can be obtained with resampled SAR images at a coarser spatial resolution, mainly because of a greater speckle reduction [15]. Finally, all features were converted to a logarithmic scale (decibels, dB) in order to enhance their visualization.

The last five evaluated approaches from the eleven initially proposed were the data-fusion combinations. We followed a simple but effective data-fusion approach that is mostly used with the Sentinel 1 and 2 dataset, combining optical, thermal, and/or SAR images by resampling the images from the different sources to get the same spatial resolution (250 m), and stacking all the images from a year together [21,52,53]. This way, each pixel contains properties and qualities extracted from the different spectral regions and the temporal information of each feature [54]. Following this method, we formulated the five combinations of features: (vii) SAR + VI map [4,55], (viii) SAR + PHENO map [56], (ix) SAR + SRB map [57,58], (x) SAR + DST map [59], and (xi) VI + DST map [60,61].

#### 2.4. Reference Data and Classification Algorithm

In the present study, we used the pixel-based Random Forest (RF) classifier, a non-parametric statistical model that creates a combination of uncorrelated decision trees based on random samples of predictors or variables [7,28]. RF is capable of managing a large number of variables in a fast and robust way, selecting the most important ones for the differentiation among categories [57,62,63]. We chose the RF algorithm since it has been reported to perform better than, for example, the Support Vector Machine, when coarse-spatial-resolution images are used [64].

Using high-spatial-resolution images from Google Earth and Bing Maps, and following a stratified random sampling, we gathered regions of interest (ROIs) of ground truth data for training the classification algorithm and to validate the results (Figure 1b). We looked for the three main land-cover types in the region: forest (natural and forest plantation), palm plantation (industrial and small scale), and low vegetation (pasture, grassland, annual crop). We used the manual digitizing method, specifically the on-screen digitizing process, which consists of manually choosing and drawing the ROIs on the high-resolution images. These areas were selected under two criteria: (1) the source image must have been taken between the year 2016 and 2018, and (2) the land cover must have remained unchanged during the study period.

Around 5000 sample points were obtained from the ROIs; half of them were used as a training dataset (1050 points of forest cover, 800 points of palm plantation, and 655 points of low vegetation), and the other half for validation. All non-vegetative cover (i.e., cities, main rivers, and aquaculture farms) were masked due to their marginal presence in the area of study and to avoid classification errors. These areas were identified with the Map of Homogeneous Accessibility Areas of the Ministry of Agriculture of Ecuador [65].

An accuracy assessment was performed by using the Overall Accuracy (OA), the Kappa coefficient, the Producer's Accuracy (PA), and the User's Accuracy (UA) [66,67]. However, our main concern was to obtain a high PA and UA for the palm plantation class, since, ideally, we should have fewer palm plantation pixels omitted from the correct class and also fewer mislabeled in other classes [68].

An overview of the workflow, with the preprocessing of the images and the classification steps to produce the thematic maps, is presented in Figure 2.

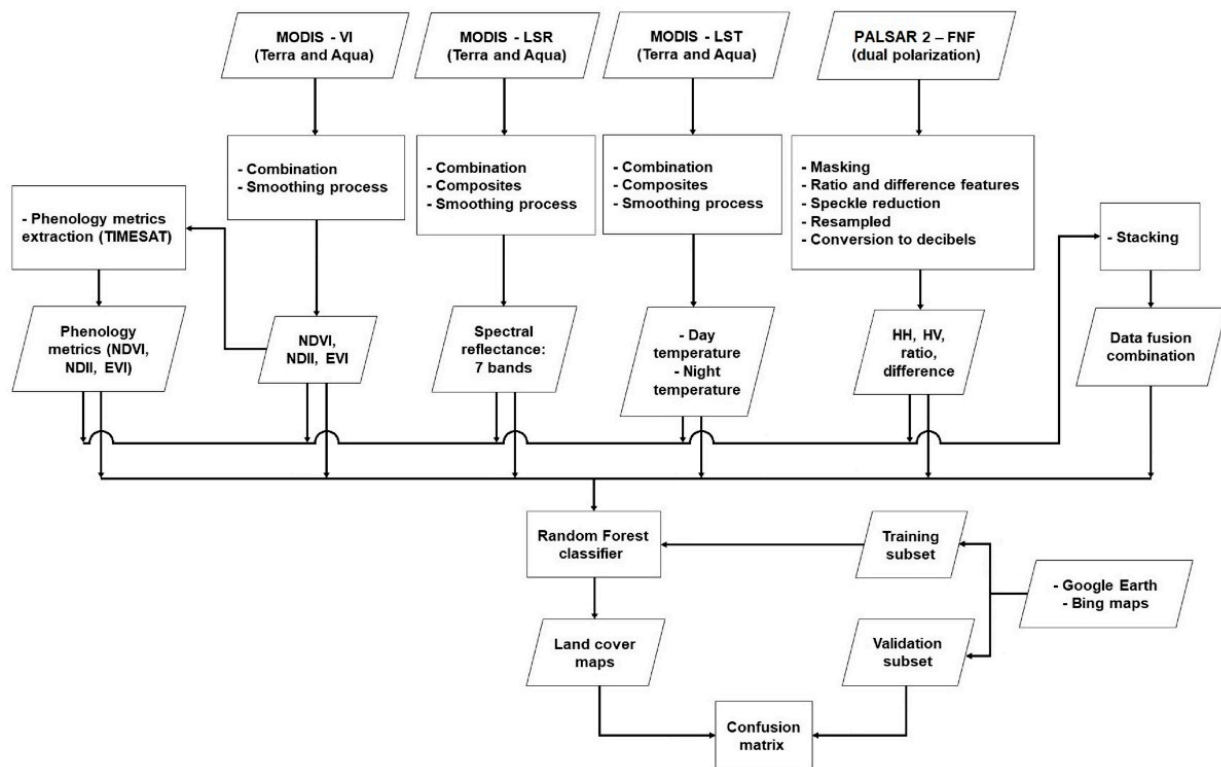


**Figure 2.** Image preprocessing workflow and classification scheme with the entire dataset. Please note that “combination” refers to the use of both image sources (Terra and Aqua satellites), while “composite” refers to the combination of images from different dates.

### 3. Results

For the first analysis, we compared the accuracy obtained by the maps created with 2017 data, recognized as the period with regular precipitation regimes (Figure 3; Table 2). It is noticeable that all the annual classification maps displayed a similar distribution of the land-cover types over the area of study.

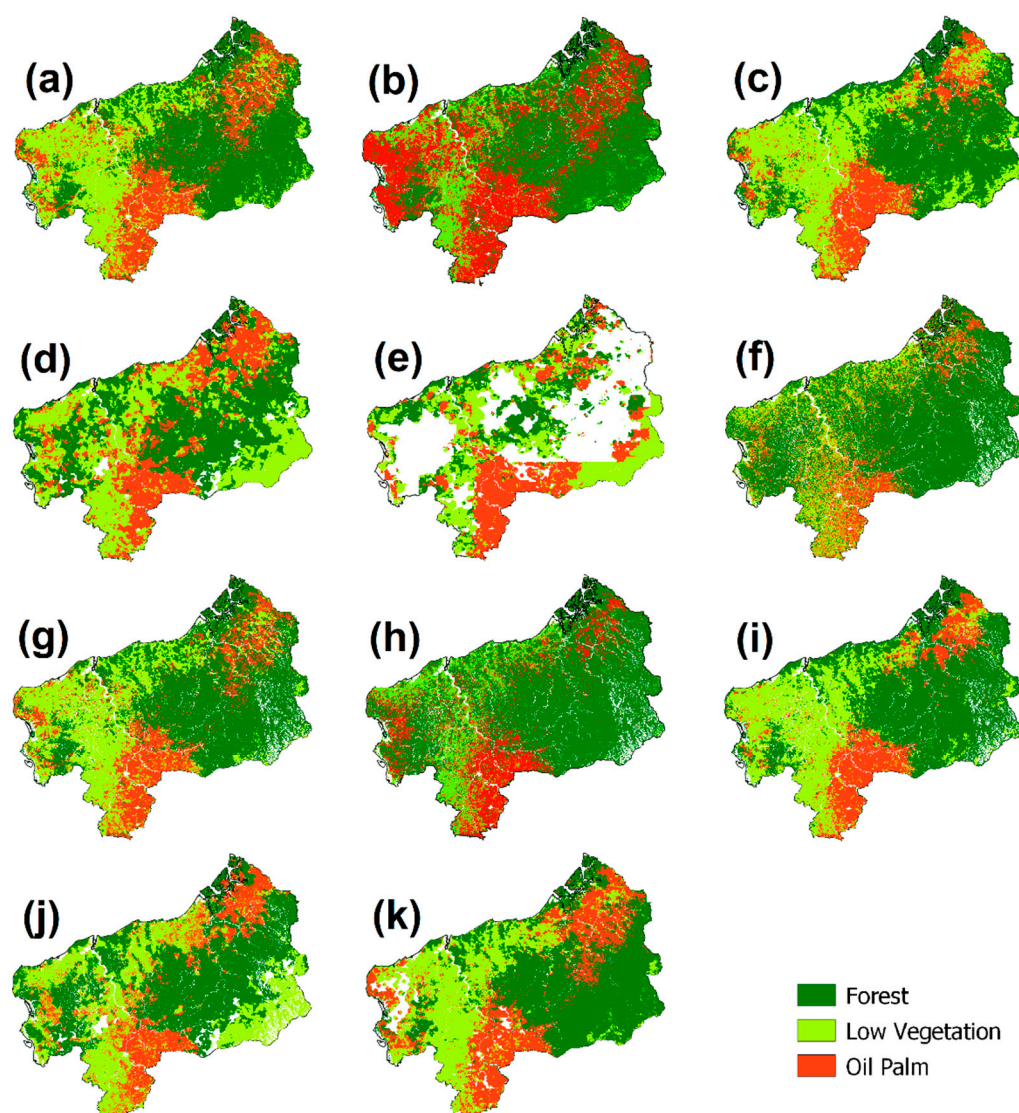


**Figure 3.** Land-cover maps of the year 2017 based on optical, thermal, and microwave features and data-fusion combinations. (a) Vegetation Indices (VIs) map; (b) Phenology metrics (PHENO) map; (c) Spectral Reflectance Bands (SRBs) map; (d) Daytime Surface Temperature (DST) map; (e) Nighttime Surface Temperature (NST) map; (f) Synthetic Aperture Radar (SAR) map; (g) SAR + VI map; (h) SAR + PHENO map; (i) SAR + SRB map; (j) SAR + DST map; and (k) VI + DST map.



**Table 2.** Accuracy metrics obtained from each approach across the three years analyzed. The metrics are Overall Accuracy (OA), Kappa coefficient (Kappa), Producer’s Accuracy (PA), and User’s Accuracy (UA). The listed approaches are Vegetation Indices (VIs), Phenology metrics (PHENO), Spectral Reflectance Bands (SRBs), Daytime Surface Temperature (DST), Synthetic Aperture Radar (SAR), and five data-fusion combinations.

			OA (%)	Kappa	PA Forest (%)	UA Forest (%)	PA Low Vegetation (%)	UA Low Vegetation (%)	PA Palm (%)	UA Palm (%)
Optical, Thermal, and Microwave Feature Maps	VI maps	2016	84.1	0.75	92.6	86.6	74.2	87.7	80.6	77.9
		2017	91.7	0.87	96.2	91	88.4	94.7	88.1	90.3
		2018	87.6	0.81	95.8	87.8	74.5	92.1	87	84.2
	PHENO maps	2016	67.2	0.49	83.1	75.1	35.7	75.6	71.4	54.8
		2017	88	0.81	95.3	85	86.4	95	79.2	87.3
		2018	70.8	0.54	87.3	87.8	74.5	92.1	87.1	84.2
	SRB maps	2016	90.1	0.85	97.3	92.7	70.7	93.9	96.4	84.4
		2017	94.6	0.92	98.4	95.4	86	94.9	96.5	93.1
		2018	89.8	0.84	97.9	87.4	75.2	96	90.5	89.3
	DST maps	2016	93.7	0.9	98	97.8	84.9	93.7	94.9	88.1
		2017	92.9	0.89	96.3	97.6	88.2	85.5	92.1	92.8
		2018	91.4	0.87	96.6	93.3	77.3	94	96.2	87.2
	NST maps	2016	87.9	0.78	85.9	98.6	75.4	86.4	94.8	86.3
		2017	82.8	0.74	77.7	92.4	74.6	64.7	96	87.6
		2018	76.5	0.65	81.7	66.9	56.6	77.8	90.4	83.6
	SAR maps	2016	87.1	0.8	96.8	90.9	71.3	86.6	86.9	82
		2017	87.1	0.8	97.2	92.1	74.1	83.2	83.8	82.7
		2018	84.8	0.77	93.7	90.8	70.7	79.8	84.2	80
Data-Fusion Combination Maps	SAR + VI maps	2016	90.8	0.86	98.3	92.9	78.5	92.8	90.4	86.2
		2017	95.3	0.93	98.6	95	90.9	96.9	93.9	93.9
		2018	93.1	0.89	97.9	94.6	85.7	93.3	92.6	90.9
	SAR + PHENO maps	2016	81.1	0.7	98.5	83.4	45.8	98.1	86.4	72.2
		2017	87.9	0.81	99.4	93.3	89.9	98	92.5	94.5
		2018	86.8	0.79	98.1	85.7	65.5	95.4	89	83.8
	SAR + SRB maps	2016	92.7	0.89	98.9	94.3	77	96.2	97.2	88.2
		2017	96.5	0.95	99.2	89.9	98.2	97.3	97.1	94.8
		2018	92.1	0.88	98.7	89.9	80	97.3	93	91.9
	SAR + DST maps	2016	95.8	0.94	99.3	99	90	94.7	95.9	92.3
		2017	95.5	0.93	98	98.9	92	90.9	94.8	94.6
		2018	93.9	0.91	97.9	95.2	83.5	95.3	97.3	91.1
	VI + DST maps	2016	92.3	0.88	94.5	98.6	86	90.3	94.4	85.8
		2017	95.3	0.93	96.9	97	90.8	96.8	96.8	91.7
		2018	92.3	0.88	97.8	95	79.4	93	95.6	88.2

### 3.1. Classification Performance of Maps from Single Data Source and Data Fusion

Comparing the maps created by using the different features from the optical spectral region, we observed that the SRB map obtained the highest OA (94.6%; Table 2) and Kappa (0.92), and also the highest PA (96.5%) and UA (93.1%) for the palm plantation class. It is, however, noteworthy how the irregularity of the topography affects the classification of the low vegetation class, due to the incorrect assignment of this class in an area of protected natural forest located in the southeast region of Esmeraldas (Figure 3c). On the other hand, the PHENO map displayed a much larger number of pixels assigned to the palm plantation class (Figure 3b), especially at the west side of the area of study, and, consequently, the lowest accuracy (OA of 88% and Kappa of 0.81) from the optical-based maps.

The DST map obtained high OA (92.9%; Table 2) and Kappa (0.89), and high PA (92.1%) and UA (92.8%) for the palm plantation class, similar to the SRB map results. Likewise, it is observable how the DST map (as well as the NST map) is affected by irregularities in the topography, similar to the case of the SRB map, but to a greater extent. Moreover, both DST and NST maps are greatly affected by cloud cover (Figure 3d,e), even after preprocessing the LST images to decrease the amount of missing values. In the NST maps, almost half

of the area of study was impacted by cloud cover, leaving no data to be analyzed. This resulted in a bias in the metrics obtained from the accuracy assessment, which obtained a high OA (82.8%) and Kappa (0.74), but, as a consequence of the massive presence of blank spaces, leaving just few pixels to validate the map. For this reason, the NST map was discarded for further analysis.

The SAR map presented a high OA (87.1%; Table 2) and Kappa (0.80), but contrary to our expectations, its accuracy was not the best one when compared to the optical and thermal feature maps. This might be due to the speckle effect that persisted in the input images even after the preprocessing steps and was consequently reproduced in the final map (Figure 3f).

Finally, all data-fusion combinations obtained higher accuracy metrics than the ones obtained from the maps created by using each data source individually (Figure 3g–k; Table 2). However, our data-fusion approach, while straightforward, also allowed the issues inherent to each data source to remain in the resulting maps. For instance, combinations using thermal data are still highly impacted by irregular topography and also presented missing data due to cloud-cover contamination (Figure 3j,k). In yet another example, maps that were created from the optical or thermal data together with SAR features kept the missing data in the southeast region of the area of study due to shadow and overlay problems (Figure 3g–j).

### 3.2. Inter-Annual Comparison of Classification Performance

To test how differences in precipitation regimes could affect palm plantation mapping, we generated a map for each year between 2016 and 2018, knowing that these three years were subjected to distinct precipitation regimes (mainly due to ENSO events in 2016 and 2018). For this analysis, we did not use the maps PHENO, PHENO + SAR, and NST, due to their low performance when compared with the rest of the optical-based maps and with the DST map, respectively (Table 2). We also did not use the SAR maps because, as mentioned before, they are the only map that follow a single-date approach, and the source images were specifically chosen to be the least affected by rainfall and surface moisture. For these reasons, SAR maps presented a high stability across the years. We focused on the best maps of the previous analysis, comparing the accuracy metrics that take into account all classes together: OA and Kappa coefficient. We chose three maps from the single-data-source approach (i.e., VI, SRB, and DST maps) and three from the data-fusion approach (i.e., SAR + SRB, SAR + DST, and VI + DST maps).

The images for each one of the tested approaches and over the three years analyzed are presented in Supplementary Figures S1 and S2, and the actual values for the OA, Kappa, and per-class accuracy metrics (i.e., PA and UA) are presented in Table 2.

Both the OA and Kappa varied across the three years analyzed (Figure 4) when comparing the performance for distinct years within approaches. Overall, the year 2017 presented the best results (except for the SAR + DST, and DST maps, for which the 2016 classification presented higher accuracies). Even for the classifications that retrieved the highest accuracies (e.g., VI, SRB, DST, VI + DST, SAR + SRB, and SAR + DST), the metrics changed from one year to another (with differences in the OA as low as 0.4%, and as high as 7.6% across the three years analyzed). It is also noteworthy that, following Landis and Koch (1977) nomenclature to label Kappa values, all output maps achieved excellent results, reaching “substantial” and “almost perfect” categories [69,70].

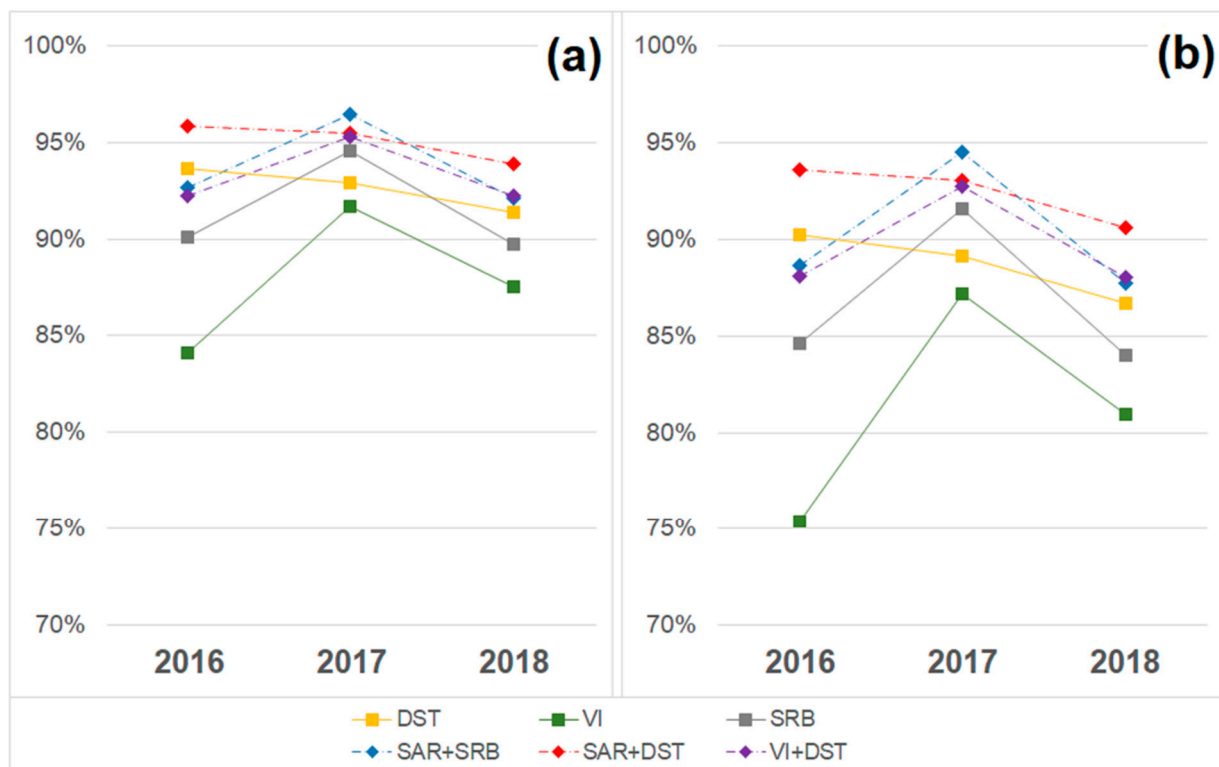


**Figure 4.** (a) Overall Accuracy and (b) Kappa coefficient for the best classification maps from the different approaches proposed across the three years analyzed. Full lines represent approaches using features from a single spectral region, while dashed lines represent data-fusion approaches.

Next, for a more comprehensive analysis of the changes produced by inter-annual climate variability in land-cover mapping, we evaluated the PA and the UA of each class in the produced maps across the three years analyzed (Figure 5) as a way of better comparing per-class accuracy [68,70].

Overall, the maps which used optical data in the single-region-feature approach and in the data-fusion approach (VI, SRB, and SAR + SRB) displayed a similar behavior: the accuracy was higher in 2017, the year with a regular precipitation regime, and lower during drought years (2016 and 2018; Supplementary Figure S1). The maps involving thermal features (DST and SAR + DST) presented a non-uniform behavior, presumably not driven by changes in precipitation regimes.

SAR data in the data-fusion approaches (SAR + SRB and SAR + DST) contributed to reduce the differences of PA and UA values of the palm plantation class among the years analyzed. For instance, in the SRB map of the year 2017, the PA value of the palm plantation class decreased by 0.1% in 2016 and 6% in 2018, and the UA decreased by 8.7% in 2016 and 3.8% in 2018. Meanwhile, in the SAR + SRB maps, the PA value obtained in the year 2017 increased by 0.1% in 2016 and decreased by 4.1% in 2018, and the UA value decreased by 6.6% in 2016 and 2.9% in 2018.

In yet another example, the PA value of the palm plantation class of the DST map of 2017 increased by 2.8% in 2016 and 4.1% in 2018, and the UA value decreased by 4.7% in 2016 and 5.6% in 2018. Meanwhile, in the SAR + DST map, the PA of the year 2017 increased by 1.1% in 2016 and 2.5% in 2018, and the UA value decreased by 2.3% in 2016 and 3.5% in 2018.

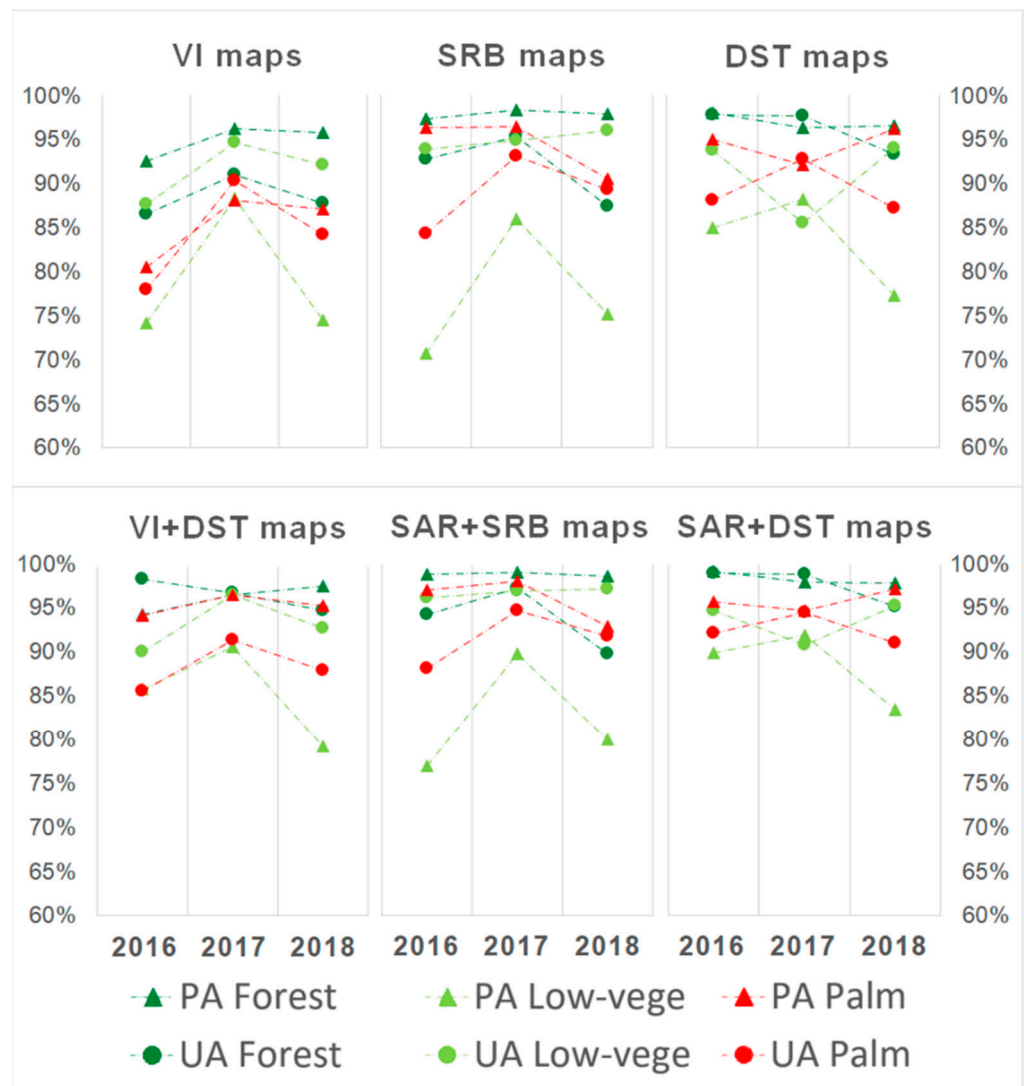


**Figure 5.** Comparison of Producer's Accuracy (PA) and User's Accuracy (UA) of the three land-cover types over the three-year analysis of the selected thematic maps (i.e., the maps with the highest OA and Kappa, three maps created by using single-data-sources approach and three with data-fusion approach).

However, data-fusion-approach maps still displayed differences among years. For example, Figure 6a shows the capture of a Google Earth image of an area corresponding to low vegetation cover unchanged from 2015 to 2018; Figure 6b shows that, in the SAR + SRB maps, the classifier assigned the palm plantation class in almost half of the pixels in the years 2016 and 2018, while, in the year 2017, the land cover is correctly assigned. Figure 6c displayed also in the year 2016 a great number of pixels assigned to the palm plantation class in the middle-west of the area of study, while those same pixels were assigned mainly as low vegetation in the other two maps (2017 and 2018).

Finally, since we focused on the accuracy obtained specifically for mapping palm plantation, we averaged the values of the two class-specific accuracy measurements, PA and UA, to obtain the mean accuracy value for the palm plantation class (hereafter, mean accuracy). This combined measure will give us an idea of the number of pixels correctly assigned to this class and the number of pixels mislabeled at the same time [15].

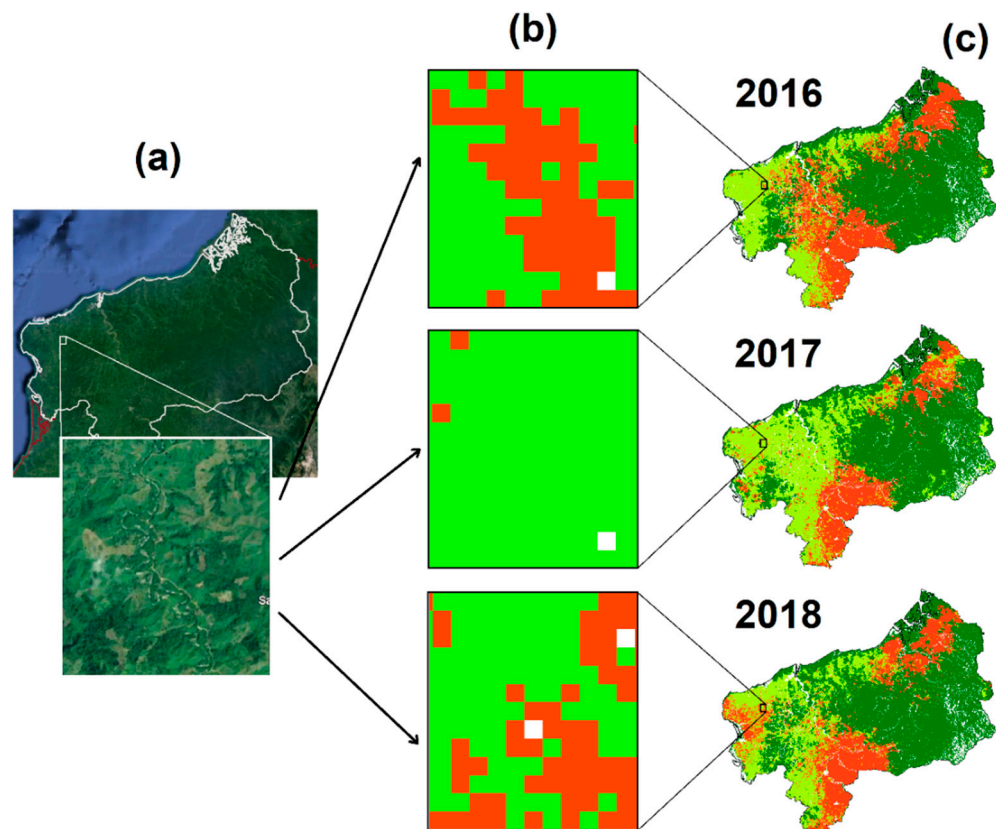


**Figure 6.** (a) True color satellite image of the area of study, with an enlarged square area dominated by low vegetation. (b) Enlargement of the classification map corresponding to the area of the square panel of the image (a). (c) SAR + SRB classification maps of the three years analyzed. The enlargement square of the 2017 map corresponds with the real land-cover type, while, in 2016 and 2018, the pixels were incorrectly assigned mostly as palm plantation.

This analysis suggested that all selected maps performed better during the year 2017 (Figure 7). For instance, the SAR + SRB maps obtained the highest mean accuracy, with an average error of only 4.5% in 2017, which rose to 7.4% in 2016 and 2018 due to the impact of inter-annual climate variability. On the other hand, the SAR + DST map obtained high and consistent mean accuracies across the three years (94.1%, 94.7%, and 94.2% in the year 2016, 2017, and 2018, respectively). That represents an error margin between 6.9% and 6.3%.



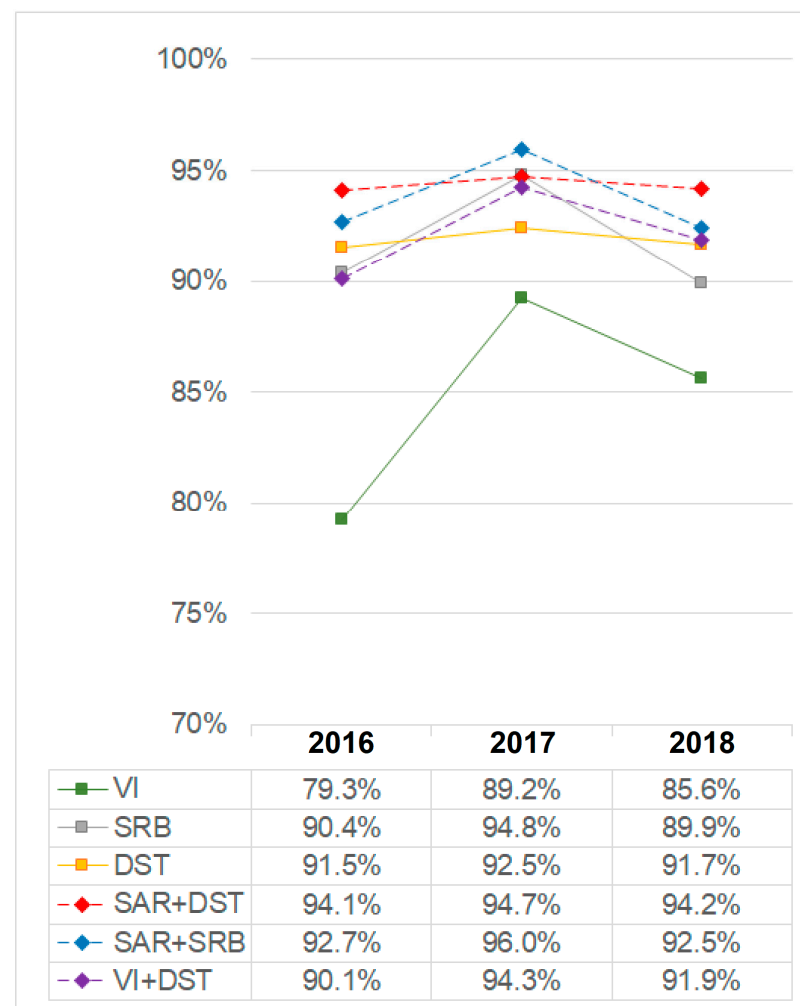


**Figure 7.** Annual differences in the mean accuracy value  $((PA + UA)/2)$  for the palm plantation class across the three years analyzed. Values are presented for each one of the previously selected approaches. Full lines represent approaches using features from a single spectral region, while dashed lines represent data-fusion approaches.

#### 4. Discussion

In this study, we provided insights on land-cover mapping accuracy obtained by using different features of the electromagnetic spectrum and some data-fusion combinations. By correctly preprocessing the available images and decreasing the amount of missing data due to cloud cover, we generated thematic maps with three land-cover types with good Overall Accuracies. However, it is noteworthy that the inter-annual climate variability affected the vegetation in such a way that it produced changes in its spectral properties during the years analyzed, resulting in inaccuracies in land-cover mapping.

The low vegetation class showed the lowest accuracy and the lowest consistency over the years when compared to the other classes. This is a consequence of the mixture of vegetation cover that this class contains (e.g., annual crops, shrubs, grassland, pasture, and bare lands), which translates into a high spectral and structural diversity. The forest class achieved the highest PA and UA in all maps, and this is in line with several other mapping studies [4,7,15,16,71], suggesting that this class is relatively easy to be separated from the other classes. In this sense, contrary to what was reported in other studies, we obtained a high spectral differentiation between the forest and the palm plantation classes [7,72]. Additionally, drastic differences in surface backscatter and temperature between palm plantation areas and forest were found [11,12,16,43]. This was potentially a consequence of the type of forest (i.e., native) that has more homogeneous characteristics than secondary

forest, and the type of palm plantation (i.e., industrial) that is more uniform (in terms of canopy closure and vertical structure) than small plots from individual farmers [7,72].

The maps generated from optical features are evidently the most affected by inter-annual climate variability, presenting the greatest differences in PA and UA for all classes among the years analyzed (Table 2 and Figure 5). For instance, in the VI map of the year 2017, the PA value of the palm plantation class decreased 7.5% in 2016 and 1.1% in 2018, and the UA decreased 12.4% in 2016 and 6.1% in 2018.

For palm plantation mapping, the SRB map showed to be the most accurate one (averaging over the three years, the map presented a PA of 94.5% and UA of 88.9%). However, it also presented a notable reduction in the accuracy for all classes during drought years. For example, when comparing the PA and UA of the forest class, the PA and the UA of the year 2016 increased 1.1% and 2.7%, respectively, in the year 2017; the same happened with the low vegetation class, as the PA and UA values increased 15.3% and 1%, respectively; and in the case of the palm plantation class, the PA and UA increased 0.1% and 8.7%, respectively (Table 2 and Figure 5). This is presumably because drought can cause physiological reactions in the vegetation, affecting photosynthetic activity and, thus, the spectral characteristics of the vegetation [27].

The VI-based thematic maps also obtained high accuracy and a distribution of the land-cover types comparable to the SRB maps (Figure 4 and Supplementary Figure S1a). However, contrary to what the literature reports regarding normalized indices compensating for changes in illumination, topographic conditions, and viewing angle, and thus producing better maps than the ones made by spectral data [8], our VI maps did not present better results than the SRB maps (although they were indeed less affected by the irregular topography).

The thematic maps generated with the phenology metrics were the least accurate and, by far, the most affected by inter-annual climate variability (Table 2 and Supplementary Figure S1b). This is understandable due to the close link between the intra-annual climatic conditions (e.g., precipitation regime, solar radiation, and temperature) and the phenology of the vegetation [8,9].

Persistent cloud cover affected most thematic maps that were based on thermal features (Supplementary Figure S1d,e). As already mentioned, the algorithm used to generate MODIS imagery is unable to retrieve LST information if the pixel does not meet certain criteria, such as clear-sky conditions [73]. Thus, since the RF classifier cannot handle missing values [74], this results in blank spots where data are missing. However, the DST maps did present a high PA and UA for the palm plantation class (averaging over the analyzed period a PA of 94.4% and a UA of 89.4%) and also obtained consistent results for all other classes (Table 2 and Figure 4). This could be a consequence of using 8-day average composites basemaps that were created from the daily measurements, but mostly because, when creating the monthly composites, we removed all the variability added by daily energy balances, rainfall events, or soil moisture, while keeping only the seasonal variability that is linked mostly to land-cover types [19,73]. The DST maps were also highly affected by the topography (e.g., irregular slope conditions and shades) present in the southeast limit of Esmeraldas province [75], creating some confusion in the classifier (Supplementary Figure S1d).

The microwave-based thematic maps showed high PA and UA for the palm plantation class (averaging over the three-year period, a PA of 85% and a UA of 81.6) but lower than the optical and thermal-based maps. Nonetheless, it obtained highly consistent results across the study period (Table 2). This is because PALSAR data are considered to be very stable in forested areas, and also as a consequence of the preselection of the SAR images that integrate the global mosaic of the FNF product used in our analysis. The selection of those images took into account seasonality and were taken annually from June to September or from November to January, preferably selecting the ones with lower surface moisture influence [44].

Our data-fusion approach integrates the features from different spectral regions to enhance information contained in each pixel and improve land-cover differentiation and classification. This way, we have additional information coming from each land cover, adding biophysical attributes to the spectral characteristics of the vegetation [18,20,76]. All data-fusion combinations presented improved OA, Kappa, and within-class accuracy (PA and UA) when compared to the ones generated without data fusion. However, they followed a similar pattern as their original data sources when comparing classification stability among the three years (Figure 5). For instance, the maps generated by using the SAR + SRB data fusion were the most accurate in terms of palm plantation classification, but still with a clear variability over different precipitation regimes, which was also the case for the SRB maps (Table 2; Figures 4 and 5). Similarly, the SAR + DST maps obtained the second highest accuracy for the palm plantation class, with more consistent results over the three-year period; this was also the case for the DST maps (Table 2; Figures 4 and 5). On top of that, all data-fusion-based maps displayed a combination of the issues present in the maps created by using each one of their data sources. For instance, all maps with SAR features contained missing values in the southeast areas due to shadow and lay-over problems on irregular topography (Supplementary Figure S2a–d). Likewise, all maps generated with LST data have topography issues and missing values due to cloud contamination (Supplementary Figure S2d,e).

Finally, with the analysis of the mean accuracy value (Figure 7), we obtained a clear idea of the impact caused by inter-annual climate variability in palm plantation mapping. As an illustration, the SAR + DST maps have virtually the same accuracy over the three years, i.e., ~6% of error. In other words, there is a 6% chance of failing to find palm plantations where they actually exist. This error margin was reduced to only 3.5% with the SAR + SRB map, under regular climate conditions (in 2017), but the accuracy decreased over altered conditions (i.e., ~7.5% of error in both 2016 and 2018).

Consequently, we here argue that inter-annual climate variability should be considered during land-cover classification, especially if the output will be used as input in further studies, for example, for the determination of plantation area or yield [77].

The present study was limited to palm plantation mapping due to its high relevance for the global economic growth and its impact in tropical forests. However, future research could perform similar analyses by using different perennial (or even with annual) crops of high importance in tropical areas. This study was also limited to a specific location, but broader scale analysis and studies in other regions that present different atmospheric mechanisms that influence vegetation response are also relevant, both to expand our knowledge and improve land-cover-mapping techniques.

## 5. Conclusions

Palm plantations, established in tropical rainforest areas, can be mapped with high accuracy, using features from all regions of the electromagnetic spectrum. Our results showed that data fusion combinations can provide a substantial improvement in the Overall Accuracy of the maps. However, the Overall Accuracy and Kappa coefficient alone are not the proper metrics to study, in detail, palm-plantation-mapping accuracy. Instead, the Producer's and User's Accuracy (and also the average of both) allowed us to determine the impact of annual climatic disturbances in palm-plantation mapping.

Our results also suggest that the effect of inter-annual climate variability over vegetation, producing changes in its spectral properties, can lead to mapping inaccuracies.

Thematic maps generated from optical features outperformed thermal and microwave-based maps in terms of Overall Accuracy, but they were the most affected by changing climatic conditions. Thermal features proved to be the most consistent against changes in rainfall regimes, but they were highly affected by persistent cloud cover, as is typical of some tropical regions. Data-fusion combination increased Overall Accuracy and inter-annual consistency in all maps, producing the highest accuracy with the SAR + SRB maps

and the highest stability with the SAR + DST maps (i.e., error margin between 3.5 and 7.5% for the former and an average error of ~6% over the three years analyzed for the latter).

We propose that further studies should take into consideration the effect of climate variability over land-cover classification, especially knowing that phenomena such as the ENSO event will occur more frequently and intensively in the future [25]. Potentially, future studies could also use change detection techniques and trend analysis to help in the differentiation of land-cover types.

**Supplementary Materials:** The following supporting information can be downloaded at <https://www.mdpi.com/article/10.3390/rs14133104/s1>. Figure S1: Land-cover maps based on optical, thermal, and microwave features across the three years analyzed. Figure S2: Land-cover maps based on data fusion combinations across the three years analyzed.

**Author Contributions:** Conceptualization, F.T. and B.S.; methodology, F.T.; software, F.T.; validation, F.T. and B.S.; formal analysis, F.T.; investigation, F.T.; resources, F.T.; data curation, F.T.; writing—original draft preparation, F.T.; writing—review and editing, B.S. and P.N.B.; visualization, F.T. and P.N.B.; supervision, B.S.; project administration, F.T.; funding acquisition, F.T. All authors have read and agreed to the published version of the manuscript.

**Funding:** This research was funded by National Secretariat of Higher Education, Science, Technology, and Innovation of Ecuador (SENESCYT; contract number CZ05-001245-2018). P.N. Bernardino is funded by the Research Foundation Flanders (grants G0F6922N and G063420N).

**Data Availability Statement:** Not applicable.

**Acknowledgments:** The authors would like to thank Jos Van Orshoven, and Guido Wyseure for the support provided in the realization of this research project.

**Conflicts of Interest:** The authors declare no conflict of interest.

## References

- De Petris, S.; Boccardo, P.; Borgogno-Mondino, E. Detection and characterization of oil palm plantations through MODIS EVI time series. *Int. J. Remote Sens.* **2019**, *40*, 7297–7311. [\[CrossRef\]](#)
- Vijay, V.; Pimm, S.L.; Jenkins, C.N.; Smith, S.J. The Impacts of Oil Palm on Recent Deforestation and Biodiversity Loss. *PLoS ONE* **2016**, *11*, e0159668. [\[CrossRef\]](#)
- Gutiérrez-Vélez, V.H.; DeFries, R.; Pinedo-Vásquez, M.; Uriarte, M.; Padoch, C.; Baethgen, W.; Fernandes, K.; Lim, Y. High-yield oil palm expansion spares land at the expense of forests in the Peruvian Amazon. *Environ. Res. Lett.* **2011**, *6*, 044029. [\[CrossRef\]](#)
- Cheng, Y.; Yu, L.; Xu, Y.; Liu, X.; Lu, H.; Cracknell, A.P.; Kanniah, K.; Gong, P. Towards global oil palm plantation mapping using remote-sensing data. *Int. J. Remote Sens.* **2018**, *39*, 5891–5906. [\[CrossRef\]](#)
- Pohl, C. Mapping palm oil expansion using SAR to study the impact on the CO<sub>2</sub> cycle. *IOP Conf. Ser. Earth Environ. Sci.* **2014**, *20*, 12012. [\[CrossRef\]](#)
- Razali, S.M.; Marín, A.; Nuruddin, A.A.; Shafri, H.Z.M.; Hamid, H.A. Capability of Integrated MODIS Imagery and ALOS for Oil Palm, Rubber and Forest Areas Mapping in Tropical Forest Regions. *Sensors* **2014**, *14*, 8259–8282. [\[CrossRef\]](#)
- Lee, J.S.H.; Wich, S.; Widayati, A.; Koh, L.P. Detecting industrial oil palm plantations on Landsat images with Google Earth Engine. *Remote Sens. Appl. Soc. Environ.* **2016**, *4*, 219–224. [\[CrossRef\]](#)
- Jin, Y.; Sung, S.; Lee, D.K.; Biging, G.S.; Jeong, S. Mapping Deforestation in North Korea Using Phenology-Based Multi-Index and Random Forest. *Remote Sens.* **2016**, *8*, 997. [\[CrossRef\]](#)
- Wardlow, B.D.; Egbert, S.L. A comparison of MODIS 250-m EVI and NDVI data for crop mapping: A case study for southwest Kansas. *Int. J. Remote Sens.* **2010**, *31*, 805–830. [\[CrossRef\]](#)
- Nooni, I.K.; Duker, A.; Van Duren, I.; Addae-Wireko, L.; Jnr, E.O. Support vector machine to map oil palm in a heterogeneous environment. *Int. J. Remote Sens.* **2014**, *35*, 4778–4794. [\[CrossRef\]](#)
- Sabajo, C.R.; le Maire, G.; June, T.; Meijide, A.; Rouspard, O.; Knohl, A. Expansion of oil palm and other cash crops causes an increase of the land surface temperature in the Jambi province in Indonesia. *Biogeosciences* **2017**, *14*, 4619–4635. [\[CrossRef\]](#)
- Ramdani, F.; Moffiet, T.; Hino, M. Local surface temperature change due to expansion of oil palm plantation in Indonesia. *Clim. Chang.* **2014**, *123*, 189–200. [\[CrossRef\]](#)
- Li, M.; Liew, S.C.; Kwok, L.K. Producing cloud free and cloud-shadow free mosaic from cloudy IKONOS images. In Proceedings of the IGARSS 2003—2003 IEEE International Geoscience and Remote Sensing Symposium, Toulouse, France, 21–25 July 2003; pp. 3946–3948. [\[CrossRef\]](#)
- Tseng, D.-C.; Tseng, H.-T.; Chien, C.-L. Automatic cloud removal from multi-temporal SPOT images. *Appl. Math. Comput.* **2008**, *205*, 584–600. [\[CrossRef\]](#)

15. Cheng, Y.; Yu, L.; Xu, Y.; Lu, H.; Cracknell, A.P.; Kanniah, K.; Gong, P. Mapping oil palm extent in Malaysia using ALOS-2 PALSAR-2 data. *Int. J. Remote Sens.* **2017**, *39*, 432–452. [CrossRef]
16. Li, L.; Dong, J.; Tenku, S.N.; Xiao, X. Mapping Oil Palm Plantations in Cameroon Using PALSAR 50-m Orthorectified Mosaic Images. *Remote Sens.* **2015**, *7*, 1206–1224. [CrossRef]
17. Oon, A.; Ngo, K.D.; Azhar, R.; Ashton-Butt, A.; Lechner, A.; Azhar, B. Assessment of ALOS-2 PALSAR-2L-band and Sentinel-1 C-band SAR backscatter for discriminating between large-scale oil palm plantations and smallholdings on tropical peatlands. *Remote Sens. Appl. Soc. Environ.* **2018**, *13*, 183–190. [CrossRef]
18. Hong, G.; Zhang, A.; Zhou, F.; Brisco, B. Integration of optical and synthetic aperture radar (SAR) images to differentiate grassland and alfalfa in Prairie area. *Int. J. Appl. Earth Obs. Geoinf. ITC J.* **2014**, *28*, 12–19. [CrossRef]
19. Lambin, E.F.; Ehrlich, D. Combining vegetation indices and surface temperature for land-cover mapping at broad spatial scales. *Int. J. Remote Sens.* **1995**, *16*, 573–579. [CrossRef]
20. Lambin, E.F.; Ehrlich, D. International Journal of Remote Sensing The surface temperature-vegetation index space for land cover and land-cover change analysis. *Int. J. Remote Sens.* **1996**, *17*, 463–487. [CrossRef]
21. Lopes, M.; Frison, P.; Durant, S.M.; Bühne, H.S.T.; Ipavec, A.; Lapeyre, V.; Pettorelli, N. Combining optical and radar satellite image time series to map natural vegetation: Savannas as an example. *Remote Sens. Ecol. Conserv.* **2020**, *6*, 316–326. [CrossRef]
22. Sarzynski, T.; Giam, X.; Carrasco, L.; Lee, J.S.H. Combining Radar and Optical Imagery to Map Oil Palm Plantations in Sumatra, Indonesia, Using the Google Earth Engine. *Remote Sens.* **2020**, *12*, 1220. [CrossRef]
23. Yusoff, N.M.; Muharam, F.M.; Khairunniza-Bejo, S. Towards the use of remote-sensing data for monitoring of abandoned oil palm lands in Malaysia: A semi-automatic approach. *Int. J. Remote Sens.* **2016**, *38*, 432–449. [CrossRef]
24. Ramdani, F. Recent expansion of oil palm plantation in the most eastern part of Indonesia: Feature extraction with polarimetric SAR. *Int. J. Remote Sens.* **2018**, *40*, 7371–7388. [CrossRef]
25. Vicente-Serrano, S.M.; Aguilar, E.; Martínez, R.; Martín-Hernández, N.; Azorin-Molina, C.; Sanchez-Lorenzo, A.; El Kenawy, A.; Tomás-Burguera, M.; Moran-Tejeda, E.; López-Moreno, J.I.; et al. The complex influence of ENSO on droughts in Ecuador. *Clim. Dyn.* **2016**, *48*, 405–427. [CrossRef]
26. Poveda, G.; Álvarez, D.M.; Rueda, Ó.A. Hydro-climatic variability over the Andes of Colombia associated with ENSO: A review of climatic processes and their impact on one of the Earth's most important biodiversity hotspots. *Clim. Dyn.* **2010**, *36*, 2233–2249. [CrossRef]
27. Fatin, M.N.; Razali, S.M.; Ahmad, A.A.; Shafri, Z.M.S.M. Oil palm dry season analysis based on moderate-resolution imaging spectroradiometer (MODIS) satellite indices. *Int. J. Remote Sens.* **2019**, *40*, 7663–7678. [CrossRef]
28. Furumo, P.R.; Aide, T.M. Characterizing commercial oil palm expansion in Latin America: Land use change and trade. *Environ. Res. Lett.* **2017**, *12*, 024008. [CrossRef]
29. Rival, L. The meanings of forest governance in Esmeraldas, Ecuador. *Oxf. Dev. Stud.* **2003**, *31*, 479–501. [CrossRef]
30. Ortiz, S.Y.C.; Valencia, K.L.P.; Estacio, J.R. Presión-Estado-Respuesta en la gestión de las áreas protegidas de la provincia de Esmeraldas. *Gestión Ambient.* **2019**, *17*, 21–22.
31. Movimiento Mundial por los Bosques Tropicales, El Amargo Fruto de la Palma Aceitera: Despojo y Deforestación. Movimiento Mundial por los Bosques Tropicales. 2001. Available online: [http://wrm.org.uy/es/files/2013/04/El\\_amargo\\_fruto\\_de\\_la\\_palma\\_aceitera.pdf](http://wrm.org.uy/es/files/2013/04/El_amargo_fruto_de_la_palma_aceitera.pdf) (accessed on 10 January 2021).
32. USAID. Innovación Productiva en el Ecuador Aceite de Palma. *Innov. Product. Ecuad.* **2013**, *4*, 1689–1699. Available online: <https://core.ac.uk/download/pdf/235988344.pdf> (accessed on 10 January 2021).
33. Ministerio de Agricultura y Ganadería. Cifras Agroproductivas. Available online: <http://sipa.agricultura.gob.ec/index.php/cifras-agroproductivas> (accessed on 5 January 2021).
34. Provincia de Esmeraldas-Geografía del Ecuador Enciclopedia del Ecuador. Available online: <http://www.encyclopediadelecuador.com/geografia-del-ecuador/provincia-de-esmeraldas/> (accessed on 5 January 2021).
35. Funk, C.; Peterson, P.; Landsfeld, M.; Pedreros, D.; Verdin, J.; Shukla, S.; Husak, G.; Rowland, J.; Harrison, L.; Hoell, A.; et al. The climate hazards infrared precipitation with stations—A new environmental record for monitoring extremes. *Sci. Data* **2015**, *2*, 150066. [CrossRef] [PubMed]
36. Provincia de Esmeraldas (Ecuador)-EcuRed. Available online: [https://www.ecured.cu/Provincia\\_de\\_Esmeraldas\\_\(Ecuador\)](https://www.ecured.cu/Provincia_de_Esmeraldas_(Ecuador)) (accessed on 6 January 2021).
37. Erfanian, A.; Wang, G.; Fomenko, L. Unprecedented drought over tropical South America in 2016: Significantly under-predicted by tropical SST. *Sci. Rep.* **2017**, *7*, 5811. [CrossRef] [PubMed]
38. Petrova, D.; Rodó, X.; Sippy, R.; Ballester, J.; Mejía, R.; Beltrán-Ayala, E.; Borbor-Cordova, M.J.; Vallejo, G.M.; Olmedo, A.J.; Stewart-Ibarra, A.M.; et al. The 2018–2019 weak El Niño: Predicting the risk of a dengue outbreak in Machala, Ecuador. *Int. J. Clim.* **2020**, *41*, 3813–3823. [CrossRef]
39. MODIS Web. Available online: <https://modis.gsfc.nasa.gov/data/dataproduct/> (accessed on 5 January 2021).
40. Mas, J.-F. Aplicaciones del sensor MODIS para el monitoreo del territorio. *Educ. Divulg.* **2011**, *7*, 2.
41. Jönsson, P.; Eklundh, L. TIMESAT—A program for analyzing time-series of satellite sensor data. *Comput. Geosci.* **2004**, *30*, 833–845. [CrossRef]



42. Htitiou, A.; Boudhar, A.; Lebrini, Y.; Hadria, R.; Lionboui, H.; Benabdelouahab, T. A comparative analysis of different phenological information retrieved from Sentinel-2 time series images to improve crop classification: A machine learning approach. *Geocarto Int.* **2020**, *37*, 1426–1449. [\[CrossRef\]](#)
43. Miettinen, J.; Liew, S.C. Separability of insular Southeast Asian woody plantation species in the 50 m resolution ALOS PALSAR mosaic product. *Remote Sens. Lett.* **2010**, *2*, 299–307. [\[CrossRef\]](#)
44. Shimada, M.; Itoh, T.; Motooka, T.; Watanabe, M.; Shiraishi, T.; Thapa, R.; Lucas, R. New global forest/non-forest maps from ALOS PALSAR data (2007–2010). *Remote Sens. Environ.* **2014**, *155*, 13–31. [\[CrossRef\]](#)
45. Karlsen, S.R.; Tolvanen, A.; Kubin, E.; Poikolainen, J.; HøGda, K.A.; Johansen, B.; Danks, F.S.; Aspholm, P.; Wielgolaski, F.E.; Makarova, O. MODIS-NDVI-based mapping of the length of the growing season in northern Fennoscandia. *Int. J. Appl. Earth Obs. Geoinf.* **2008**, *10*, 253–266. [\[CrossRef\]](#)
46. Garrouette, E.L.; Hansen, A.J.; Lawrence, R.L. Using NDVI and EVI to Map Spatiotemporal Variation in the Biomass and Quality of Forage for Migratory Elk in the Greater Yellowstone Ecosystem. *Remote Sens.* **2016**, *8*, 404. [\[CrossRef\]](#)
47. Lewińska, K.E.; Ivits, E.; Scharadt, M.; Zebisch, M. Alpine Forest Drought Monitoring in South Tyrol: PCA Based Synergy between scPDSI Data and MODIS Derived NDVI and NDII7 Time Series. *Remote Sens.* **2016**, *8*, 639. [\[CrossRef\]](#)
48. Bojanowski, J.; Kowalik, W.; Bochenek, Z. Noise reduction of NDVI time-series: A robust method based on Savitzky-Golay filter. *Rocz. Geomatyki* **2009**, *7*, 13–21.
49. Wen, G.; Marshak, A.; Song, W.; Knyazikhin, Y.; Möttus, M.; Wu, D. A Relationship Between Blue and Near-IR Global Spectral Reflectance and the Response of Global Average Reflectance to Change in Cloud Cover Observed From EPIC. *Earth Space Sci.* **2019**, *6*, 1416–1429. [\[CrossRef\]](#)
50. Argenti, F.; Lapini, A.; Bianchi, T.; Alparone, L. A Tutorial on Speckle Reduction in Synthetic Aperture Radar Images. *IEEE Geosci. Remote Sens. Mag.* **2013**, *1*, 6–35. [\[CrossRef\]](#)
51. SNAP-STEP. Available online: <http://step.esa.int/main/toolboxes/snap/> (accessed on 8 January 2021).
52. Lopes, M.; Frison, P.-L.; Crowson, M.; Warren-Thomas, E.; Hariyadi, B.; Kartika, W.D.; Agus, F.; Hamer, K.C.; Stringer, L.; Hill, J.K.; et al. Improving the accuracy of land cover classification in cloud persistent areas using optical and radar satellite image time series. *Methods Ecol. Evol.* **2020**, *11*, 532–541. [\[CrossRef\]](#)
53. Kempeneers, P.; Sedano, F.; Seebach, L.; Strobl, P.; San-Miguel-Ayanz, J. Data Fusion of Different Spatial Resolution Remote Sensing Images Applied to Forest-Type Mapping. *IEEE Trans. Geosci. Remote Sens.* **2011**, *49*, 4977–4986. [\[CrossRef\]](#)
54. Orynbaikyzy, A.; Gessner, U.; Conrad, C. Crop type classification using a combination of optical and radar remote sensing data: A review. *Int. J. Remote Sens.* **2019**, *40*, 6553–6595. [\[CrossRef\]](#)
55. Torbick, N.; Salas, W.; Xiao, X.; Ingraham, P.; Fearon, M.; Biradar, C.; Zhao, D.; Liu, Y.; Li, P.; Zhao, Y. Integrating SAR and optical imagery for regional mapping of paddy rice attributes in the Poyang Lake Watershed, China. *Can. J. Remote Sens.* **2011**, *37*, 17–26. [\[CrossRef\]](#)
56. Ghazaryan, G.; Dubovyk, O.; Löw, F.; Lavreniuk, M.; Kolotii, A.; Schellberg, J.; Kussul, N. A rule-based approach for crop identification using multi-temporal and multi-sensor phenological metrics. *Eur. J. Remote Sens.* **2018**, *51*, 511–524, Correction in *Eur. J. Remote Sens.* **2018**, *51*. [\[CrossRef\]](#)
57. Zhang, X.; Wu, B.; Ponce-Campos, G.E.; Zhang, M.; Chang, S.; Tian, F. Mapping up-to-Date Paddy Rice Extent at 10 M Resolution in China through the Integration of Optical and Synthetic Aperture Radar Images. *Remote Sens.* **2018**, *10*, 1200. [\[CrossRef\]](#)
58. Laurin, G.V.; Liesenberg, V.; Chen, Q.; Guerriero, L.; Del Frate, F.; Bartolini, A.; Coomes, D.; Wilebore, B.; Lindsell, J.; Valentini, R. Optical and SAR sensor synergies for forest and land cover mapping in a tropical site in West Africa. *Int. J. Appl. Earth Obs. Geoinf. ITC J.* **2013**, *21*, 7–16. [\[CrossRef\]](#)
59. Kaplan, G.; Avdan, Z.Y.; Avdan, U. Mapping and Monitoring Wetland Dynamics Using Thermal, Optical, and SAR Remote Sensing Data. *Wetl. Manag. Assess. Risk Sustain. Solut.* **2019**, *87*, 88–89. [\[CrossRef\]](#)
60. Zhang, G.; Xiao, X.; Dong, J.; Kou, W.; Jin, C.; Qin, Y.; Zhou, Y.; Wang, J.; Menarguez, M.A.; Biradar, C. Mapping paddy rice planting areas through time series analysis of MODIS land surface temperature and vegetation index data. *ISPRS J. Photogramm. Remote Sens.* **2015**, *106*, 157–171. [\[CrossRef\]](#) [\[PubMed\]](#)
61. Xiao, H.; Weng, Q. The impact of land use and land cover changes on land surface temperature in a karst area of China. *J. Environ. Manag.* **2007**, *85*, 245–257. [\[CrossRef\]](#) [\[PubMed\]](#)
62. Gislason, P.O.; Benediktsson, J.A.; Sveinsson, J.R. Random Forests for land cover classification. *Pattern Recognit. Lett.* **2006**, *27*, 294–300. [\[CrossRef\]](#)
63. Pal, M. Random forest classifier for remote sensing classification. *Int. J. Remote Sens.* **2005**, *26*, 217–222. [\[CrossRef\]](#)
64. Sheykhou, M.; Mahdianpari, M.; Ghanbari, H.; Mohammadimanesh, F.; Ghamisi, P.; Homayouni, S. Support Vector Machine Versus Random Forest for Remote Sensing Image Classification: A Meta-Analysis and Systematic Review. *IEEE J. Sel. Top. Appl. Earth Obs. Remote Sens.* **2020**, *13*, 6308–6325. [\[CrossRef\]](#)
65. Ministerio de Agricultura y Ganadería. *Mapa de Zonas Homóneas de Accesibilidad*; Ministerio de Agricultura y Ganadería: Carchi, Ecuador, 2015; p. 81.
66. Chabalala, Y.; Adam, E.; Ali, K.A. Machine Learning Classification of Fused Sentinel-1 and Sentinel-2 Image Data towards Mapping Fruit Plantations in Highly Heterogeneous Landscapes. *Remote Sens.* **2022**, *14*, 2621. [\[CrossRef\]](#)
67. Randazzo, G.; Cascio, M.; Fontana, M.; Gregorio, F.; Lanza, S.; Muzirafuti, A. Mapping of Sicilian Pocket Beaches Land Use/Land Cover with Sentinel-2 Imagery: A Case Study of Messina Province. *Land* **2021**, *10*, 678. [\[CrossRef\]](#)

- 
68. Foody, G.M. Status of land cover classification accuracy assessment. *Remote Sens. Environ.* **2002**, *80*, 185–201. [[CrossRef](#)]
  69. Landis, J.R.; Koch, G.G. The Measurement of Observer Agreement for Categorical Data. *Biometrics* **1977**, *33*, 159–174. [[CrossRef](#)] [[PubMed](#)]
  70. Foody, G.M. Explaining the unsuitability of the kappa coefficient in the assessment and comparison of the accuracy of thematic maps obtained by image classification. *Remote Sens. Environ.* **2020**, *239*, 111630. [[CrossRef](#)]
  71. Kamiran, N.; Sarker, M.L.R. Exploring the Potential of High Resolution Remote Sensing Data for Mapping Vegetation and the Age Groups of Oil Palm Plantation. *IOP Conf. Ser. Earth Environ. Sci.* **2014**, *18*, 12181. [[CrossRef](#)]
  72. Santos, C.; Messina, J.P. Multi-Sensor Data Fusion for Modeling African Palm in the Ecuadorian Amazon. *Photogramm. Eng. Remote Sens.* **2008**, *74*, 711–723. [[CrossRef](#)]
  73. Sharma, L.D.; Kumar, M.; Gupta, J.K.; Rana, M.S.; Dangwal, V.S.; Dhar, G.M. MODIS Land Surface Temperature Products Users' Guide. *Indian J. Chem. Technol.* **2001**, *8*, 169–175.
  74. Carranza, E.J.M.; Laborte, A.G. Random forest predictive modeling of mineral prospectivity with small number of prospects and data with missing values in Abra (Philippines). *Comput. Geosci.* **2015**, *74*, 60–70. [[CrossRef](#)]
  75. Hais, M.; Kučera, T. The influence of topography on the forest surface temperature retrieved from Landsat TM, ETM + and ASTER thermal channels. *ISPRS J. Photogramm. Remote Sens.* **2009**, *64*, 585–591. [[CrossRef](#)]
  76. Sano, E.E.; Ferreira, L.G.; Huete, A.R. Synthetic Aperture Radar (L band) and Optical Vegetation Indices for Discriminating the Brazilian Savanna Physiognomies: A Comparative Analysis. *Earth Interact.* **2005**, *9*, 1–15. [[CrossRef](#)]
  77. Olofsson, P.; Foody, G.M.; Stehman, S.V.; Woodcock, C.E. Making better use of accuracy data in land change studies: Estimating accuracy and area and quantifying uncertainty using stratified estimation. *Remote Sens. Environ.* **2013**, *129*, 122–131. [[CrossRef](#)]